Brittle fracture of three-dimensional lattice structure

Huaiyuan Gu*, Anton Shterenlikht, Martyn Pavier

Department of Mechanical Engineering, University of Bristol, Queen's Building, University Walk, Bristol BS8 1TR, UK

Abstract

This work aims to develop a greater understanding of fracture behaviour of a three-dimensional lattice structure. Octet-truss lattice was used in this study due to its high strength to density ratio and great potential in the advanced lightweight structure applications. The fracture toughness, K_{IC}, was found to be almost isotropic while the modulus and strength were highly dependent on the model size and lattice orientation. The converged solution for the modulus and strength were obtained when model width is large compared to cell. The modulus can be varied by 20% and the strength can be doubled when lattice orientation was changed. The validity of linear elastic fracture mechanics(LEFM) was examined on different model geometries including single edge notch tension(SENT), compact tension(CT), single edge notch bending(SENB) and thumbnail crack model. It shows that the LEFM can be adequately used in the structures with linear crack fronts. In the thumbnail crack model, the curved crack front generates more complexity in the structure ahead of the crack tip which results in a significant discrepancy in measured toughness compared to the models with linear crack fronts. Moreover, great fracture performance was exhibited in the lattices, where an increase in fracture load was observed during the crack growth.

Keywords: lattice structure, lattice orientation, fracture toughness, tensile strength, lattice modulus, FE analysis

*Corresponding author

Email address: hg1740@bristol.ac.uk (Huaiyuan Gu)

Nomenclature

Acronyms

CT	Compact Tension
LEFM	Linear Elastic Fracture Mechanics
SENB	Single Edge Notch Bending
SENT	Single Edge Notch Tension

Greek

$\overline{\rho}$	Relative density
σ_f	Failure stress
σ_t	Tensile strength of lattice

Latin

a	Crack length
E^*	Modulus of lattices
E_s	Modulus of strut material
K_R	Fracture resistance
K_{IC}	Fracture toughness
l	Strut length
n, k	Cell width and height
P_c	Fracture load
r	Strut radius

1. Introduction

The opportunities for the use of 3D periodic lattice structures is steadily growing, for example frames, sandwich panel cores and bone replacements [1, 2, 3, 4], Complex mechanical properties, such as high strength to density ratio, negative Poisson's ratio, or high energy absorption can be achieved by a careful structural optimisation [5, 6]. Despite much recent theoretical and applied research in lattice structures, not many studies characterise the fracture performances of three dimensional lattice structures such as crack paths or load versus displacement response.

The relationship between node connectivity, Z, and macroscopic mechanical properties of lattice structures have been explored by Deshpande et al. [7] who concluded that stretch-dominated lattices with high nodal connectivity are generally more weight efficient compared to bending-dominated lattices. The effective elastic modulus of 2D and 3D lattices have been studied extensively [8, 9, 10]. In particular, the elastic modulus of the octet-truss lattice, the lattice we investigate in this work, has been evaluated [11]. The modulus of 2D triangular lattices have been found to be isotropic, while its yield strength depends significantly on orientation[12]. Similar conclusion was reached for 3D octet-truss lattices where the collapse strength varies remarkably with loading directions [13].

Mechanical properties of lattices also vary significantly with specimen size, when the macroscopic dimensions of the lattice specimen are small compared to the cell size, l, for example it has been demonstrated that the modulus and strength of 2D hexagonal lattices increases with an increase in specimen size[14]. However, the opposite trend was observed for triangular lattices, where the effective modulus reduces significantly with an increase in specimen size, reaching a saturation modulus for sufficiently large specimens[12].

The fracture toughness of 2D honeycombs has been studied using FE analysis of large circular lattice models with prescribed nodal displacements and rotations based on the Mode I asymptotic field to evaluate the lattice tough-

ness, K_{IC} [15]. This approach assumes that both the model and the crack are sufficiently large compared to the cell size, so that the lattices can be treated as a continuum. It was found that the lattice toughness was related to the material strength, σ_f, and the relative density, $\overline{\rho}$, by:

$$K_{IC} = D\overline{\rho}^d \sigma_f \sqrt{l} \tag{1}$$

where D and d are topology dependent parameters [7, 16, 17]. The fracture toughness of 3D octet-truss lattice has been measured experimentally measured using single edge notched bending (SENB) tests in [13], where it was found that the toughness scales linearly with the relative density, and the square root of the cell size. This conclusion is consistent with the behaviour of 2D triangular lattices.

The validity of LEFM for lattices was found to depend on the crack size, as demonstrated for short cracks in two dimensional honeycombs[18]. LEFM overestimated the critical strength of lattices with short cracks, but gave correct predictions for long cracks, $a/l > 7$. A similar effect was also observed in two dimensional lattice structures[17].

An increase in fracture resistance with crack length in three dimensional octet-truss lattice was reported in [13]. The crack propagation in the ductile lattices was simulated numerically for a two dimensional honeycomb and different crack growth patterns were observed for different combinations of imperfection type and topology[19]. The fracture toughness and crack path were also found to change significantly with loading orientation for two dimensional triangular lattices[12].

In this work we investigate the modulus, strength and fracture behaviour of octet-truss lattice at a specific orientation where the structure can be created by interconneting a two dimensional triangular lattice in the $x - y$ plane with regular tetrahedrons along the z-direction, as shown in Fig. 1. The unit cell dimensions are related to the cell size, l, from which the relative density is

calculated as:

$$\overline{\rho} = 6\sqrt{2}\pi(r/l)^2 \tag{2}$$

where r is the strut radius. The properties are evaluated for the three main orientations – 'orientation-X, -Y and -Z', as shown in Fig. 2. The naming of these orientations was based on the loading direction and local coordinate of the unit cell.

This paper is arranged as follows. Sec. 2 provides an analytical and numerical analysis of the strength and modulus of the lattice, including its size and orientation dependence. Sec. 3 describes the fracture toughness calculations and Sec. 4 investigates the validity of LEFM by comparing the toughness evaluated from several model geometries. Finally, Sec. 5 shows the analysis of crack propagation, crack paths and fracture response curves to demonstrate crack behaviour for different lattice orientations.

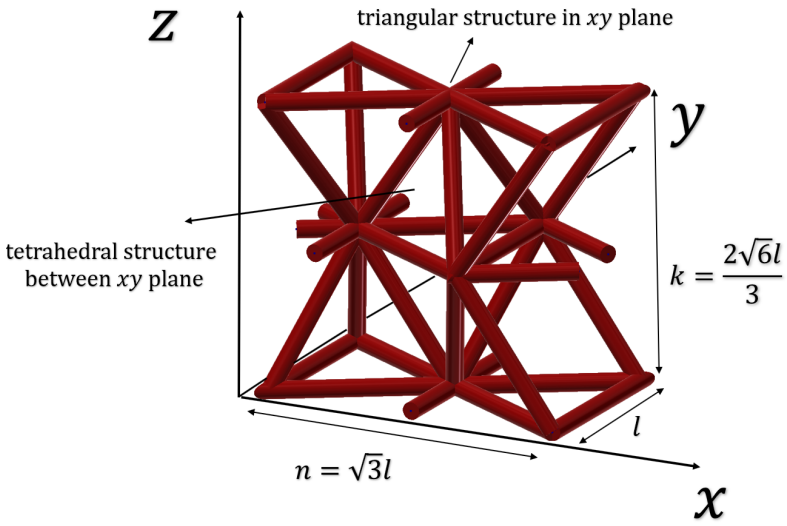

Figure 1: Configuration of unit cell structure

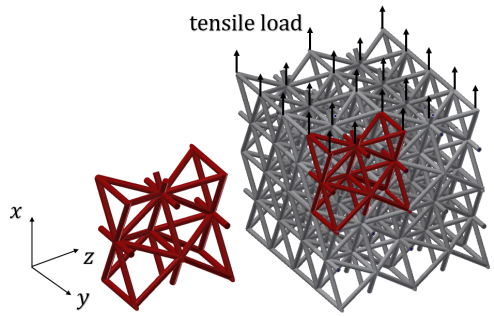

(a) orientation-X

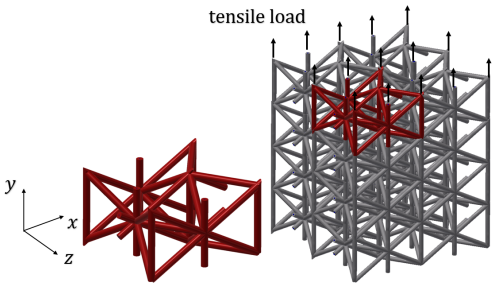

(b) orientation-Y

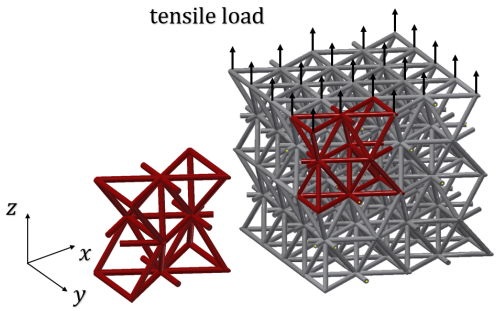

(c) orientation-Z

Figure 2: Definition of lattice orientations, based on the direction of applied tensile load.

2. Tensile strength

2.1. Analytical calculations

The octet-truss lattice is a stretch-dominated structure; hence, in the analytical model, each joint is treated as a frictionless hinge. The macroscopic load is predominantly balanced by tensile and compressive axial stresses within the struts. Previous work [20, 21, 22] has investigated the influence of the end conditions of the struts on the elastic properties of the lattice. For some geometries, rigid end conditions lead to a higher lattice modulus, but for other geometries, including the octet-truss geometry studied in this work, the end conditions have little effect. Fig. 3 shows that a change in structural orientation results in a different stress distribution within the structure, which leads to a dependence of lattice strength on orientation. Similar calculations of lattice strength to those presented here have been carried in other work [11], although using different loading directions to the ones we use.

In the orientation-X structure the strength is mainly due to the triangular structures within the $x-y$ plane, as shown in Fig. 3(a). The angled struts are under tension and the horizontal struts are in compression. The struts between the triangular structures are loaded in bending which is a second order effect for strength. When the structure is sufficiently large compared to the cell size, then the structure contained in every unit space becomes identical to that shown in Fig. 3(a). For this orientation the remote applied stress σ_∞ can be related to the axial stress in the struts σ_s by:

$$\sigma_\infty \frac{k}{2} l = 2\sigma_s \pi r^2 cos(\pi/6) \tag{3}$$

The strength of the orientation-X lattice, σ_t^X, can be obtained by substituting Eqn. (2) into Eqn. (3) and replacing the axial stress, σ_s, with the material failure stress, σ_f:

$$\sigma_t^X \approx 0.25 \overline{\rho} \sigma_f \tag{4}$$

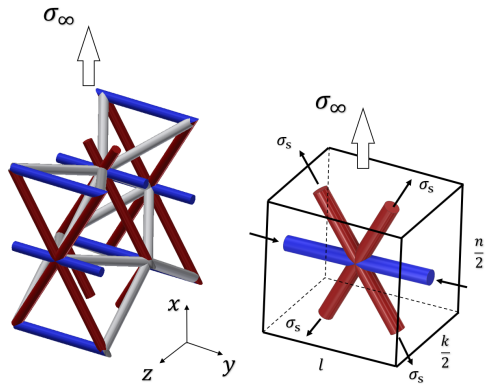

(a) orientation-X

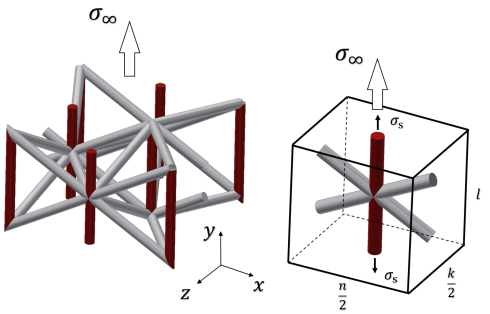

(b) orientation-Y

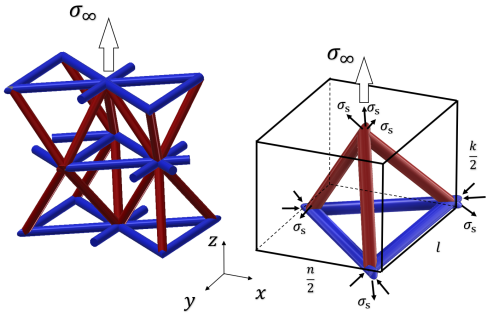

(c) orientation-Z

Figure 3: Schematic of the unit cell stress states under tension along coordinate axes. Red, blue and grey colours indicate the struts which are in tension, compression and bending respectively

In the orientation-Y structure the stress is distributed though struts which are parallel to the loading direction, see Fig. 3(b). Compared to the orientation-X and the orientation-Z structures, it had the least number of struts contributing to the strength, and the relationship between σ_∞ and σ_s can be expressed by:

$$\sigma_\infty \frac{nk}{4} = \sigma_s \pi r^2 \tag{5}$$

Thus the strength of the orientation-Y structure, σ_t^Y, can be related to the relative density and the failure stress as:

$$\sigma_t^Y \approx 0.17 \overline{\rho} \sigma_f \tag{6}$$

The orientation-Z was found to be the only orientation where the strength was contributed from all components within the structure. The triangular structures within the $x-y$ plane are under compression whereas the struts between the $x-y$ planes are under tension. Thus, the remote applied stress, σ_∞, can be expressed as:

$$\sigma_\infty \frac{nl}{2} = 3\sigma_s \pi r^2 cos(0.6\pi) \tag{7}$$

Therefore, the strength of the orientation-Z lattice, σ_t^Z, can be obtained as follows:

$$\sigma_t^Z \approx 0.34 \overline{\rho} \sigma_f \tag{8}$$

2.2. FE analysis

The analytical calculations assume that the structure is large compared to the cell size. However, in practice the structures are often made in various sizes and the results from Sec. 2.1 cannot be used adequately for small structures. The effect of the size of the structure on strength under uniaxial tensile load was investigated using the Abaqus FE system [23]. Three sets of rectangular structures were created in orientation-X, orientation-Y and orientation-Z. For

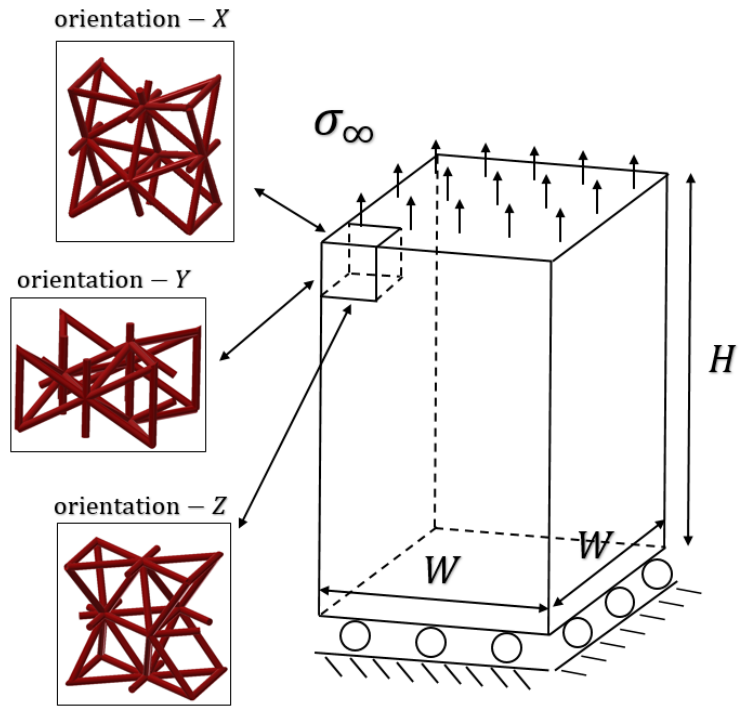

Figure 4: Rectangular FE lattice models for each of the three orientations.

each orientation the models were made with various cross sectional areas. The model width, W, ranged between approximately $3l$ to $17l$, while the height, H, was kept at $20l$ for all models, see Fig 4.

Point load was applied on each node at the top surface in the vertical direction, while vertical motion of the nodes at the bottom surface were constrained which allows displacement in the lateral direction. The strut behaviour was modelled using 10 Timoshanko beam elements for each strut (Abaqus element type B31) with linear interpolation functions. This mesh refinement was sufficient to ensure mesh independence. The strut dimensions and material properties are listed in Tab. 1.

The evaluated strength was normalised by the relative density, $\overline{\rho}$, and the material failure stress, σ_f, see Fig. 5. The orientation-Z structure was found to be the strongest. It was also found that the evaluated strengths of the

strut length, l	strut radius, r	modulus, E	Poisson's ratio, ν	failure stress, σ_f
10 mm	0.5 mm	70 GPa	0.33	140 MPa

Table 1: Strut dimensions and material properties.

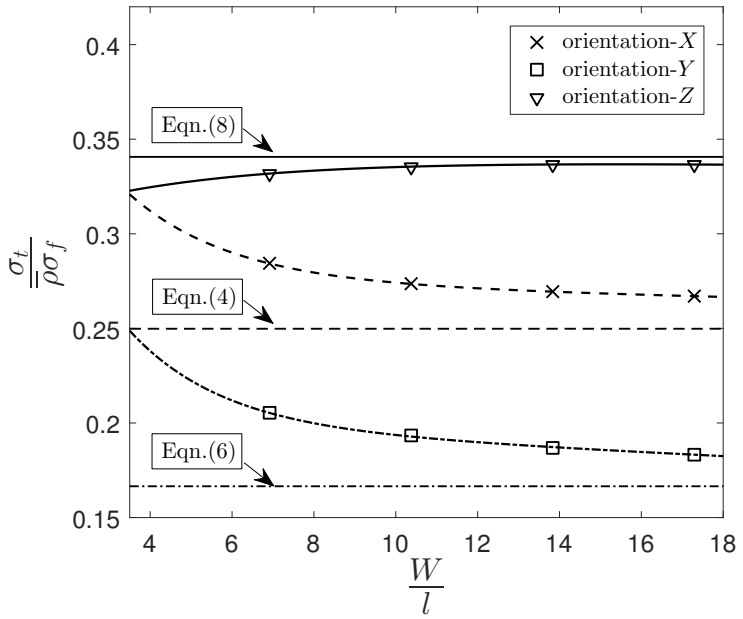

Figure 5: The normalised FE predicted strength of lattice versus normalised model size. The horizontal lines are the analytical results.

orientation-X and -Y structures were higher than the analytical prediction, caused by the finite model size. In orientation-X and orientation-Y structures the load was predominantly carried by the layers of triangular structures, shown in Figs. 3(a) and (b). The macroscopic strength, σ_t, was proportional to the ratio of the number of layers, N, to the macroscopic model width, $(N-1)k/2$, and the ratio reduces asymptotically with increasing, N.

The strength of the orientation-Z structure was relatively insensitive to the change of model width. However, a structure of this orientation shows a marked edge effect; the cells at the free edge are more compliant than the cells in the middle of the structure. This effect was only significant for $W < 10l$, where

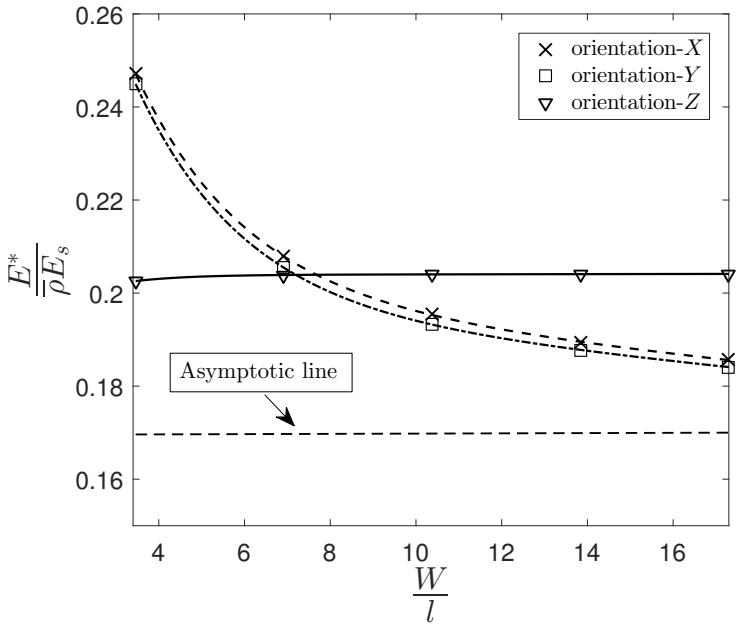

Figure 6: The normalised modulus versus normalised model size for the 3 main orientations. The horizontal line indicates the asymptotic value of the orientation-X and -Y curves.

a reduced strength is predicted. The analytical calculation of strength can be adequately used for all orientations when W is sufficiently large. The size independent strength for each orientation are shown in Tab. 2. The strength of orientation-Z is about 35% higher than that of orientation-X and double that of orientation-Y structure.

mech. prop	orientation-X	orientation-Y	orientation-Z
$E^*/(\overline{\rho}E_s)$	0.17	0.17	0.20
$\sigma_t^*/(\overline{\rho}\sigma_f)$	0.25	0.17	0.34
$K_{IC}/(\overline{\rho}\sigma_f\sqrt{l})$	0.27	0.26	0.25

Table 2: Mechanical properties of the lattice in 3 main orientations.

The elastic modulus of the lattice was also evaluated. A size effect was observed again for all orientations. The modulus is isotropic in the $x-y$ plane (due to a 6-fold symmtry), and reduces asymptotically with increasing model

width, as shown in Fig 6. The lattice modulus E^* was normalised by the material modulus, E_s, and the relative density. It was found that the modulus of orientation-X and orientation-Y models were dependent on size whereas the moduli of orientation-Z models did not change with size. The modulus of orientation-X and -Y structure can be related to model width, W, by:

$$\frac{E^*}{\overline{\rho}E_s} = 0.17(1 + \frac{3.5W/l + 2}{2.7(W/l)^2}) \tag{9}$$

This expression is derived based on calculating the equivalent moduli of the layers of triangular lattices [12]. Hence, the converged values in Table 2 for orientation-X and -Y can be predicted from the results of the finite sized FE models by taking W/l to be large. The converged value for orientation-Z structure is about 0.2 which can be obtained from the Fig.6, see Tab. 2. Furthermore, the Poisson's ratios of the lattice have also evaluated. These are found to be independent of the model size and are given by $v_{xy} = 0.33$, $v_{xz} = 0.25$ and $v_{yz} = 0.15$.

3. Fracture toughness

The fracture toughness, K_{IC}, was evaluated using single edge notch tension (SENT) models, made with the three orientations shown in Fig. 7. Uniform tension was applied at the top, while the bottom was constrained in the loading direction. The element and material properties were identical to those in Sec. 2.

Based on preliminary FE analyses with SENT models of various sizes, the model width and height were $W = 50l$ and $H = 150l$; sufficiently large achieve converged results. The ratio of the crack length, a, to the model width, W, was 0.6, where the T-stress was approximately zero[24]. Further analysis of the T-stress on lattice toughness is given in Sec. 4.

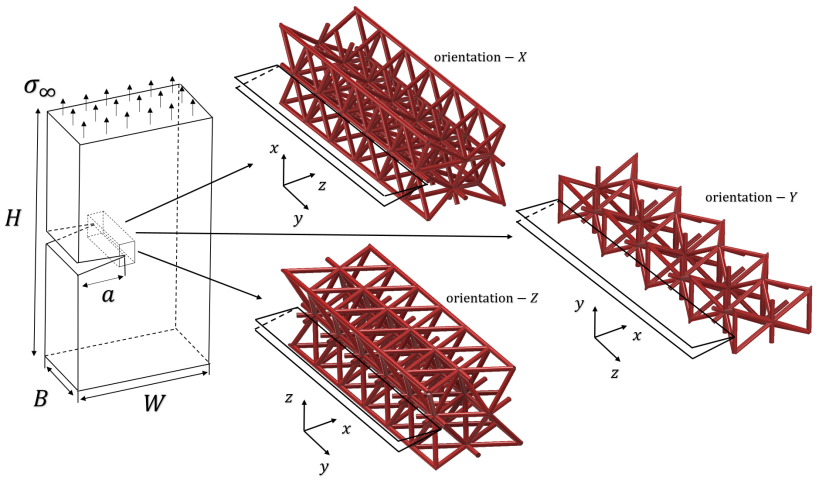

Figure 7: SENT FE model used for fracture toughness calculations, $a/W = 0.6$.

Effect of thickness, B, on toughness was measured via a systematic analysis of models with an increasing thickness. The critical strength, σ_{cr}, was taken as the applied stress which induced stress σ_f in the 1st strut ahead of the crack tip. The K_I at fracture, denoted as K_I^*, was then calculated based on the critical strength[25]:

$$K_I^* = \sigma_{cr}\sqrt{\pi a} f(a/W) \tag{10}$$

where

$$f(a/W) = 1.122 - 0.231(a/W) + 10.55(a/W)^2 - 21.71(a/W)^3 + 30.382(a/W)^4 \tag{11}$$

The results are shown in Fig. 8, where models with small number of cell through thickness show higher toughness, K_I^*, and an asymptotic behaviour is seen with increasing number of cells. This is mainly caused by the length dependence for strength of crack tip structures. The strength of the structure reduces with increasing crack depth, which is similar to the size effect demonstrated in Sec.2.2. The fracture toughness, K_{IC}, is the asymptotic limit of K_I^*, which can be seen to be less sensitive to the change of orientation than strength, as shown in Tab. 2.

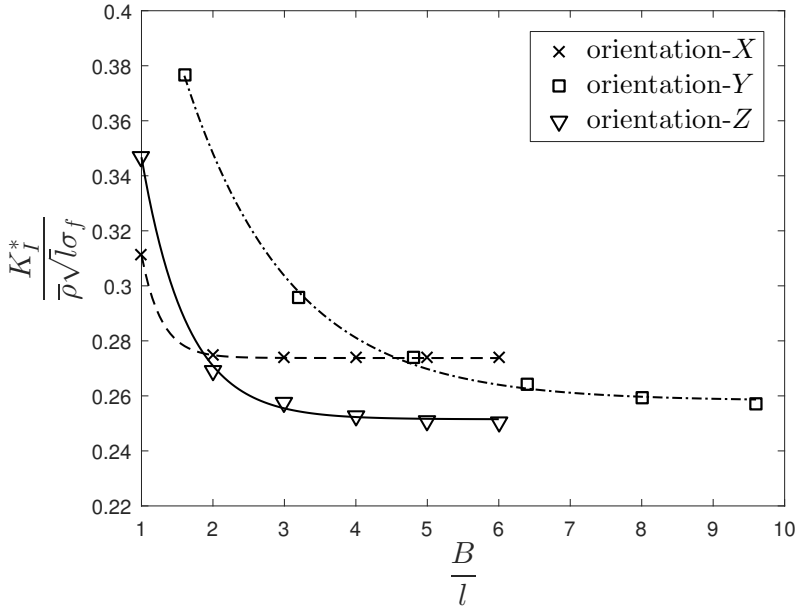

Figure 8: The thickness effect on K_I^* of the lattice

4. Model geometry effect and T-stress

The influence of the selection of model geometries on the measured toughness is investigated in this section. The toughness was evaluated from 4 geometries using orientation-Y structure: single edge notch tension(SENT), Fig. 9(a); compact tension(CT), Fig. 9(b); single edge notch bending(SENB), Fig. 9(c); and the thumbnail crack model, Fig. 10. These geometries were chosen to investigate crack tip constraint effects, quantified by the T-stress. The significance of T-stress in fracture of 2D lattice has been explored by Fleck and Qiu [17], who concluded that T-stress effects are more significant in lattice compared to conventional materials. The T-stress represents a lateral axial stress at the crack tip. It is the first non-singular term in the Williams expansion of the stresses near the crack tip in a continuum and thus has an effect only if there is a fracture process zone of finite size. The stress in the most heavily loaded strut scales linearly with the T-stress, which result in the change of toughness.

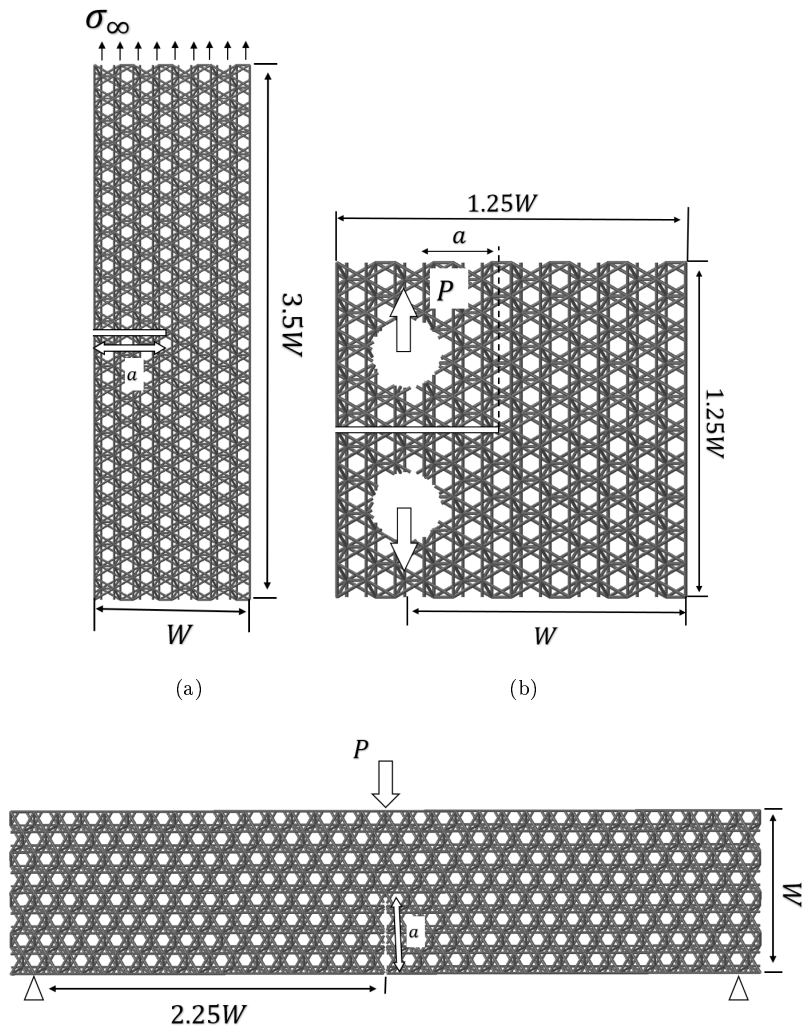

(a) (b)

(c)

Figure 9: Orientation-Y lattices created in different model geometries: (a) Single edge notched tension(SENT) (b) Compact tension(CT) (c) Single edge notched bending(SENB).

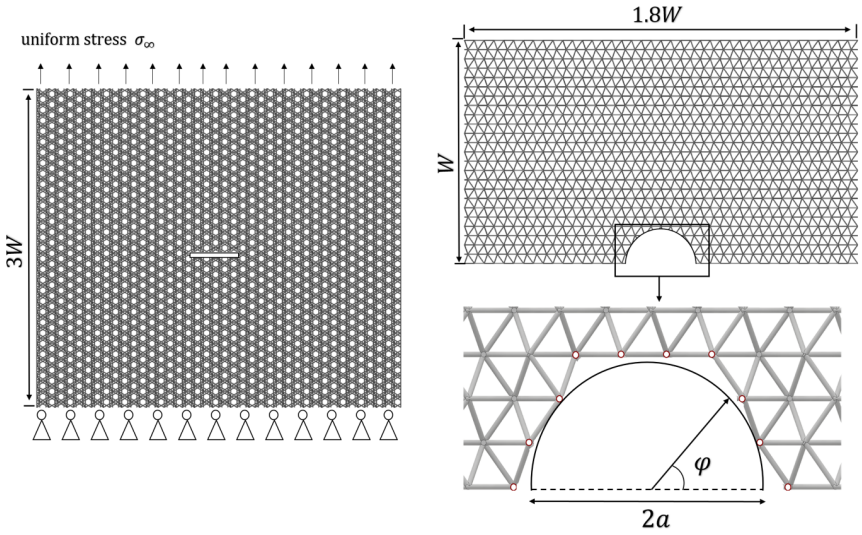

Figure 10: Thumbnail model for orientation-Y.

For the SENT model, a uniformly distributed load was applied on nodes at the top surface while the nodes at the bottom surface was constrained in the loading direction, but allowing displacement in the lateral directions. The crack length of the SENT was chosen to be half of the model width, $a/W = 0.5$. In the CT model, the motion of nodes around the pin holes are coupled to a controlling point located at the centre of each pin hole. Point loads are then applied on the controlling points to simulate conditions of a real experiment. The normalised crack length, a/W, of the CT model was chosen to be 0.38 according to the standard geometry defined by ASTM E399[26].

The deeply notched SENB model was created with $a/W = 0.5$. The two ends at the bottom surface are constrained in the vertical direction, and a point load was applied at the center of the top surface. The loading conditions applied to the thumbnail model was identical to that for the SENT model, and the crack size was chosen to be $a/W = 0.2$. The magnitude of T-stress for each model geometry is shown in Tab. 3, where the T-stress was positive for the CT and deeply notched SENB models[24, 27] and negative for the SENT and thumbnail crack models[28, 29].

	SENT	SENB	CT	thumbnail
	$a/W = 0.5$	$a/W = 0.5$	$a/W = 0.38$	$\varphi = 0$
$T/\overline{\rho}\sigma_f$	-0.012	0.016	0.015	-0.024
$K_I^*/(\overline{\rho}\sigma_f\sqrt{l})$	0.25	0.26	0.26	0.22

Table 3: Normalised T-stress and toughness for different cracked geometries.

The K_I^* of the model was calculated from the critical load using expressions given in [30]. Moreover, each model geometry was made into 5 different sizes (relative to the cell size) to evaluate the size effect on K_I^* and establish the asymptotic value of K_I^*. The results are shown in Fig. 11 where the dashed line indicates the normalised fracture toughness, K_{IC}, evaluated under the condition where the T-stress was zero, see Sec. 3. Very similar toughness values were evaluated from the SENT, SENB and CT models. However, the K_I^* obtained from the thumbnail crack model was found to be appraximately 10% lower than the K_{IC}. This indicates that a significant error will be incurred when using the K_{IC} to characterise the critical strength of the thumbnail crack model. This discrepancy is caused by the complexity of the lattice structure ahead of a nominally curved crack front, but which is discretised into a complex crack front by the lattice pattern. More specifically, the crack front structure varies along the curved crack front, which results in different tip strength compared to the linear crack front. Also, the unit cell is not axisymmetric, with regards to the vertical axis, while the global model geometry is axisymmetric. It is found that the stress in the most heavily loaded strut located at $\phi = \pi$ is approximately 20% higher than $\phi = 0$, due to the slight difference in the angles that the struts at $\phi = 0$ and $\phi = \pi$ make with the loading direction. Furthermore the toughness evaluated from the the deeply notched SENB model and CT model were found to be slightly higher than that of the SENT model which was attributed to the influence of a positive T-stress.

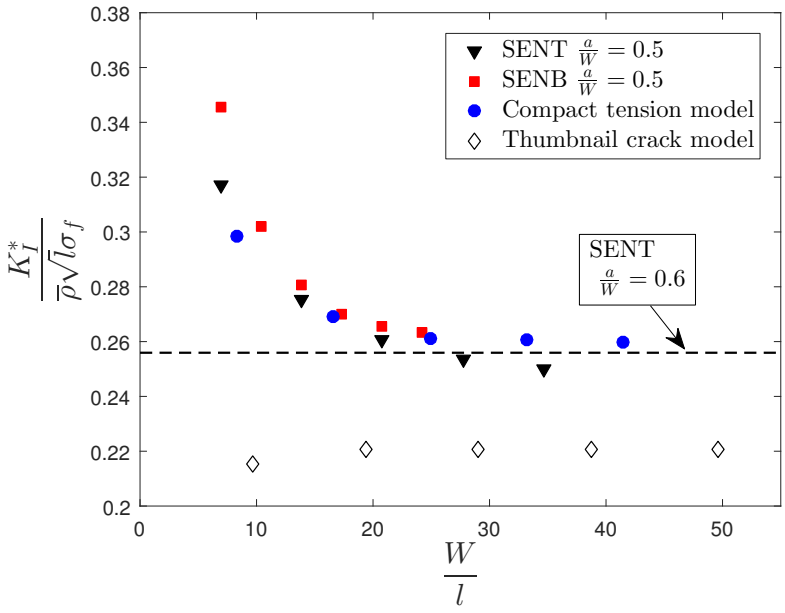

Figure 11: Scaled toughness vs model size for different geometries.

To demonstrate the effect of T-stress on K_I^* of the lattice, a modified boundary layer analysis(BLA) has been performed. Due to the large computation effort required for a large scale 3D model, 2D triangular lattice was used; a large circular triangular lattice model was created with $R = 100l$, as shown in Fig. 12, which has been found to be sufficiently large to achieve converged result [15]. The node displacements and rotations were applied to the outer boundary based on K_I asymptotic field with additional T-stress terms:

$$
\begin{aligned}
u_x(R,\theta) &= K_I \frac{1-v}{E}\sqrt{\frac{R}{2\pi}} cos(\frac{\theta}{2})(3-4v-cos(\theta)) + T\frac{1-v^2}{E} Rcos(\theta) \\
u_y(R,\theta) &= K_I \frac{1-v}{E}\sqrt{\frac{R}{2\pi}} sin(\frac{\theta}{2})(3-4v-cos(\theta)) - T\frac{v(1+v))}{E} Rsin(\theta) \\
\phi &= \frac{\partial u_x}{\partial y} - \frac{\partial u_y}{\partial x}
\end{aligned}
\tag{12}
$$

The K_I^* was evaluated for the model subjected to different magnitude of T-stress, and the results was shown in Fig. 13. It has been found that the location of the most heavily loaded strut changed from strut a to strut b when T-stress increases. When strut a is the most heavily loaded strut, an increase in T-stress results in an increase in the load carried by strut b and a reduction in the load carried by strut a, leading to an increase in K_I^*. When the T-stress is higher than the critical value, T_c, strut b becomes the most heavily loaded strut and an increase in T-stress results in an increase in the load carried by the strut, leading to a decrease in K_I^*. The critical T-stress, T_c , was indicated in Fig. 13, and the K_I^* became more sensitive to the change of T-stress for $T > T_c$.

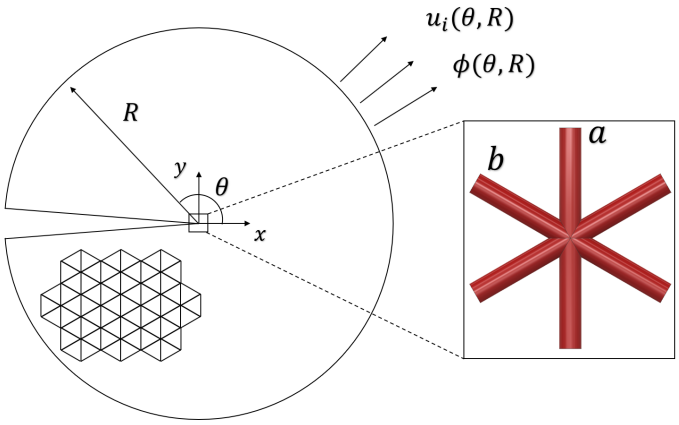

Figure 12: Boundary layer analysis of a 2D triangular lattice

5. Fracture response and crack paths

FE prediction of crack propagation carried out using the element deletion technique for orientation-X, -Y and -Z structures. Brittle fracture was simulated by reducing the element bending and axial stiffness to zero when the axial stress reached the failure stress, σ_f at an integration point. This was implemented via a user defined field variable subroutine in the Abaqus.

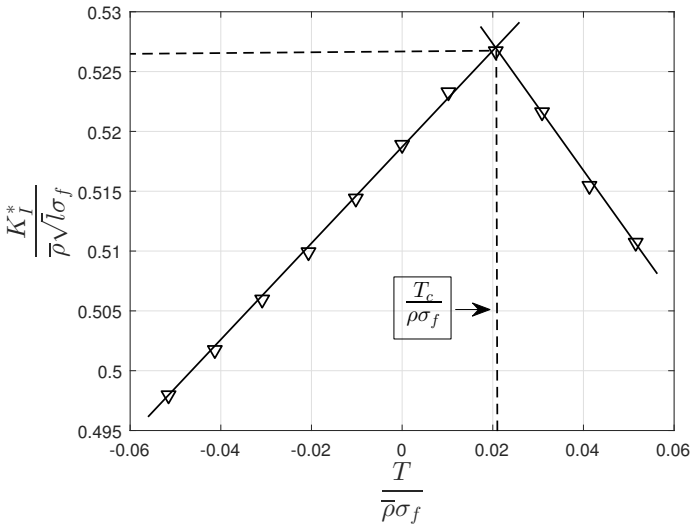

Figure 13: Two parameters fracture criterion for 2D triangular lattice structure

SENT,CT and thumbnail models were analysed. The element and material properties were identical to the previous models, see Tab. 1. In the SENT and the thumbnail models a fixed displacement was applied on the top surface, while the bottom surfaces were constrained in the loading direction.

Crack paths are shown by highlighting the failed elements in Figs. 14, 15 and 16. More detailed visualisations are given in Figs. 17 and 19. The crack path depends on both the structural orientation and geometry. In the SENT model, the crack paths of orientation-X and orientation-Z structures were perpendicular to the loading direction, see Fig. 14(a) and (c). However, the crack in the orientation-Y structure deviated from the original orientation by 30°, see Fig. 14(b). The crack path deviation was also observed in the CT model, see Fig. 15, where the crack path of the orientation-Y structure fluctuated up and down with 30° inclination. The performance of the thumbnail crack was also found to be orientation dependent. In the orientation-Y and -Z structures, the crack paths deviated from the horizontal plane, particularly in orientation-Z structure, where the crack path was conical, see Fig. 16(c).

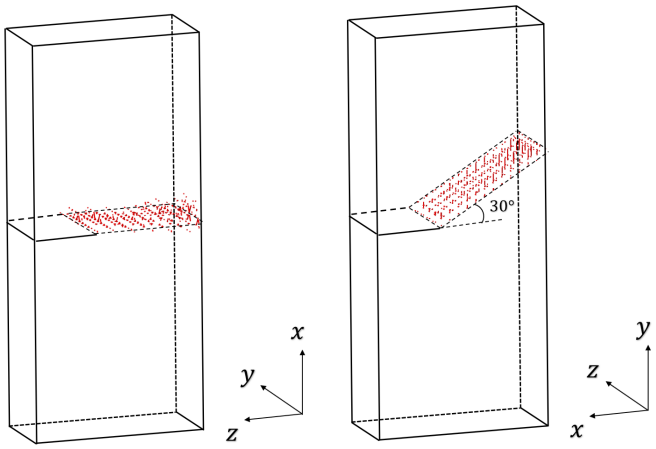

(a) orientation-X (b) orientation-Y

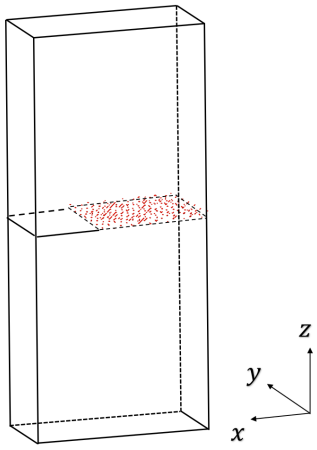

(c) orientation-Z

Figure 14: The crack paths in the SENT model created in three lattice orientations, $W = 13l$ and $a/W = 0.25$.

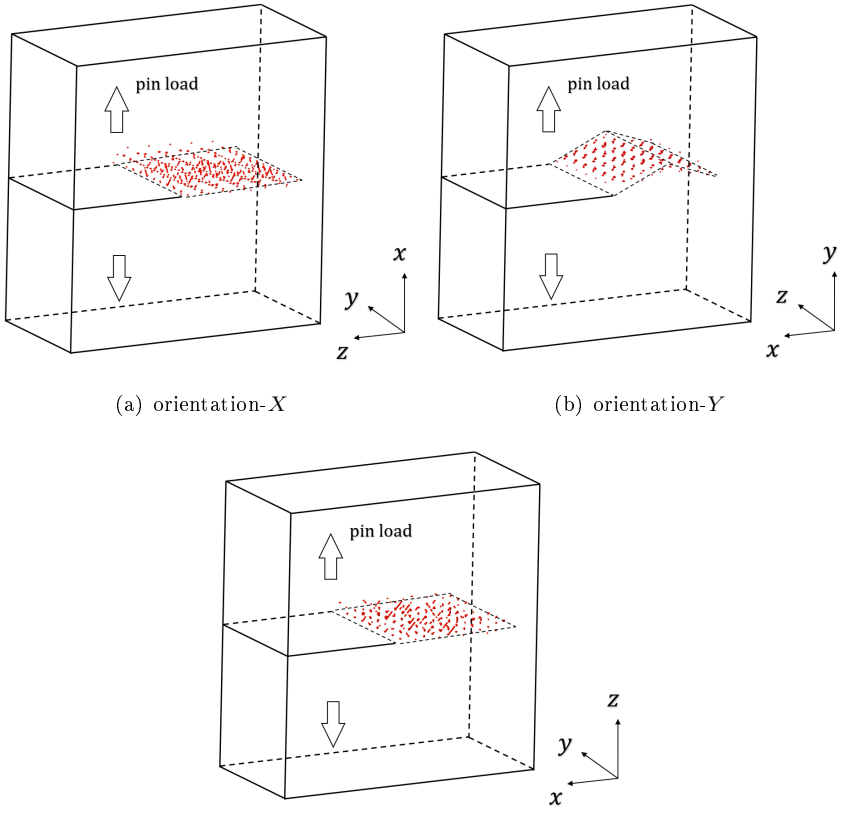

(a) orientation-X (b) orientation-Y

(c) orientation-Z

Figure 15: The crack paths in the CT model created in three lattice orientations, $W = 17l$ and $a/W = 0.38$.

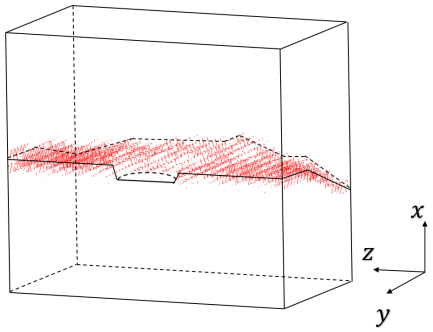

(a) orientation-X

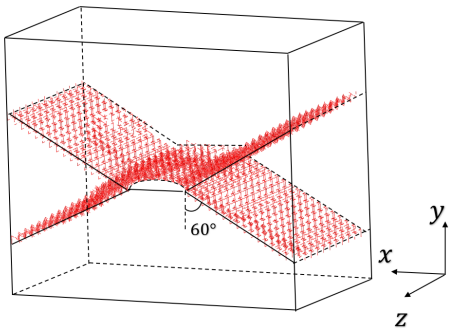

(b) orientation-Y

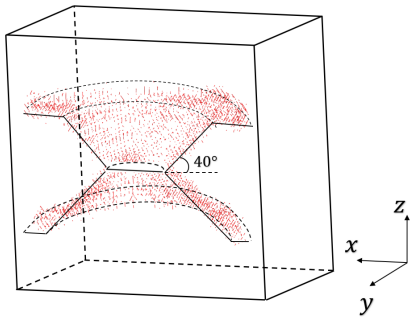

(c) orientation-Z

Figure 16: The crack paths in the thumbnail crack model created in three lattice orientations, $W = 20l$ and $a = 4l$.

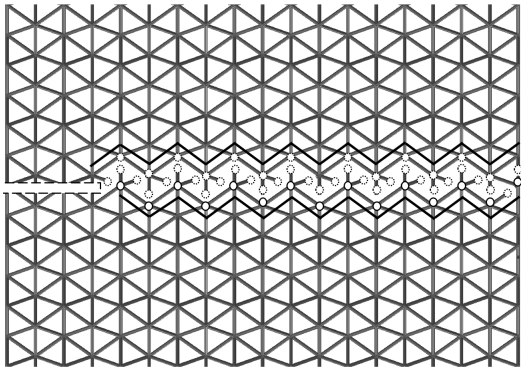

(a) orientation-X

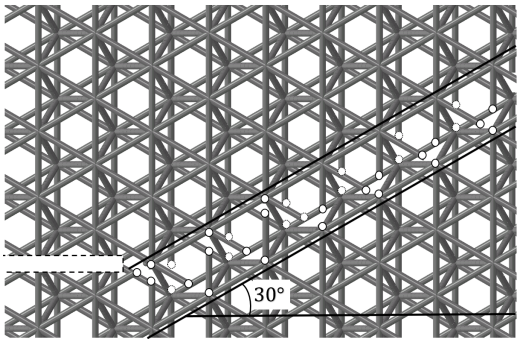

(b) orientation-Y

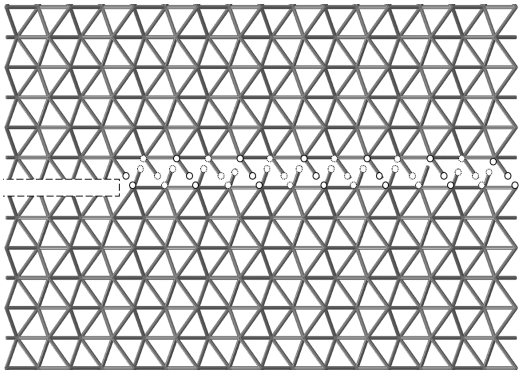

(c) orientation-Z

Figure 17: The detailed crack paths in the SENT models created in three orientations.

The fracture response curves were plotted for each orientation. There was no significant orientation dependency observed in terms of fracture load in the SENT or the CT models, as shown in Figs. 18 and 19. The pop-in effect was observed in the CT models made of orientation-X and -Z structures, where crack arrested after struts failed in front of the initial crack front, and a higher load was needed to re-start crack propagation, see Fig. 19. This was due to the change of the lattice configuration at the crack tip, where a stronger crack tip structure was formed following failure of the near tip struts. The pop-in was only seen when the structure was subjected to a bending load. In the SENT models, particularly with short cracks, the pop-in effect was small compared to the CT models.

In the thumbnail crack model, orientation-Z shows a significantly higher fracture resistance compared to the other orientations, because the initial crack propagation is along a macroscopically conical surface, leading to an increasing number of struts at the crack front. The peak nominal stress (load over the net area of the top surface) was achieved after the conical propagation stage gave way to the horizontal fracture surfaces. The fracture load of the orientation-Z model cannot be adequately characterised using the fracture toughness, K_{IC}, given in Tab. 2, which assumed the crack onset under the conditions of Mode I fracture. However, it is still unclear how much these observations are affected by limited model sizes (width and depth). The thumbnail crack model used in the simulation contains about 1600 thousand nodes and 1700 thousand elements, and a large number of increments are required to ensure the accuracy of the prediction. Thus,the fracture behaviour in larger thumbnail crack model was not conducted in this work. Open source FE solvers such as ParaFEM will be considered in the future work to reduce computation time.

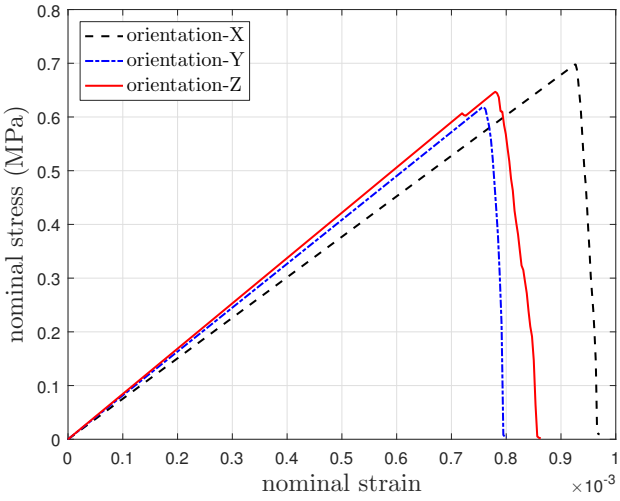

Figure 18: The fracture responses of SENT models.

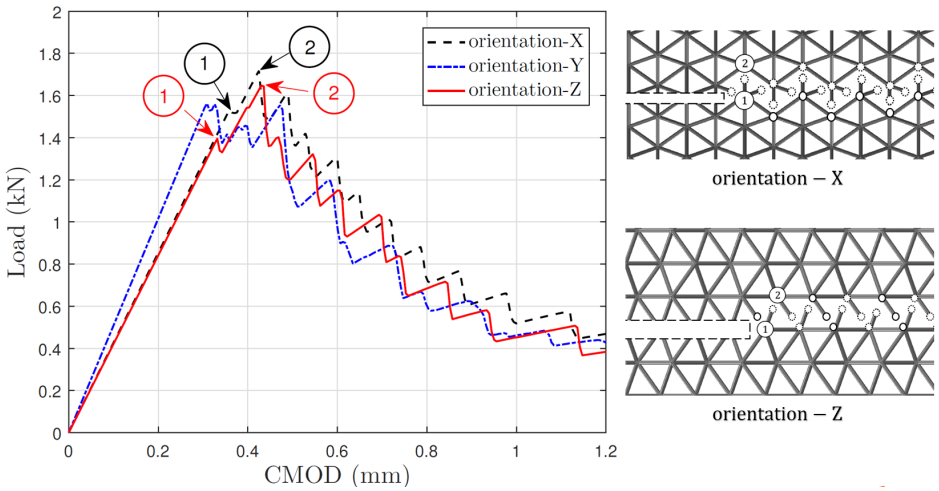

Figure 19: The fracture responses of CT models.

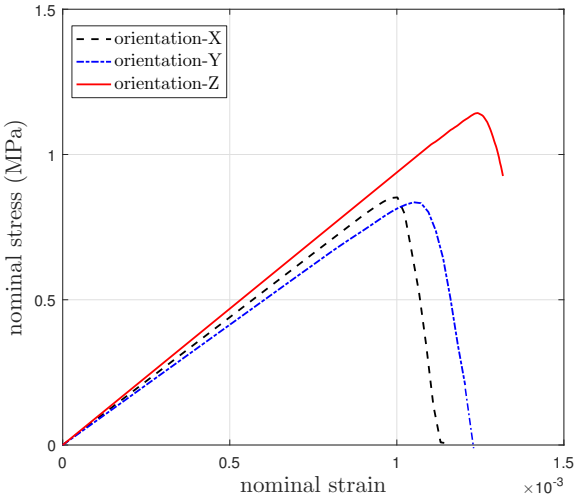

Figure 20: The fracture responses of thumbnail crack models.

The fracture resistance, K_R, of the lattice during crack extension was evaluated from the compact tension(CT) models. As shown in the Fig.19, the load-displacement curves of the CT models show zig-zag pattern. Each load drop corresponds to a crack extension and peak points indicates fracture loads, P_c, for each crack length. Compliance method was adopted to calculate the effective crack length using the expression based on ASTM E399[26]:

$$\frac{a}{W} = 1.000 - 4.500U + 13.157U^2 - 172.551U^3 + 879.944U^4 - 1514.6711U^5 \quad (13)$$

Where:

$$U = \frac{1}{1 + \sqrt{(\frac{EBV_m}{P})}} \quad (14)$$

The V_m is the crack mouth opening displacement, P the applied force, E is effective Young's modulus of the lattice model and B is the model thickness. Hence the fracture resistance, K_R, is calculated as:

$$K_R = \frac{P_c}{B\sqrt{W}} f(\frac{a}{W}) \quad (15)$$

Where the $f(a/W)$ is a geometry factor which has been defined from the previous study[30]. Fig. 21 shows the fracture resistance curves for each orientation. It was found that the initial fracture resistance evaluated from the crack growth simulation are higher than the fracture toughness prediction shown in Tab.2. This is due to the influence of model size, which is not sufficiently large to achieve the fracture toughness of the lattice.

Furthermore, it was found that the fracture resistance increases with crack size. As shown in Fig. 21, a sharp increase in K_R was observed after the initial crack growth which was caused by the pop-in effect described previously. The fracture resistance is continuously rising with further extension of the crack. This is attributed to the small initial crack size relative to the cell size, and is consistent with the fact demonstrated from the previous work on two-dimensional lattices where the measured toughness increases with crack size until a converged value was reached[18].

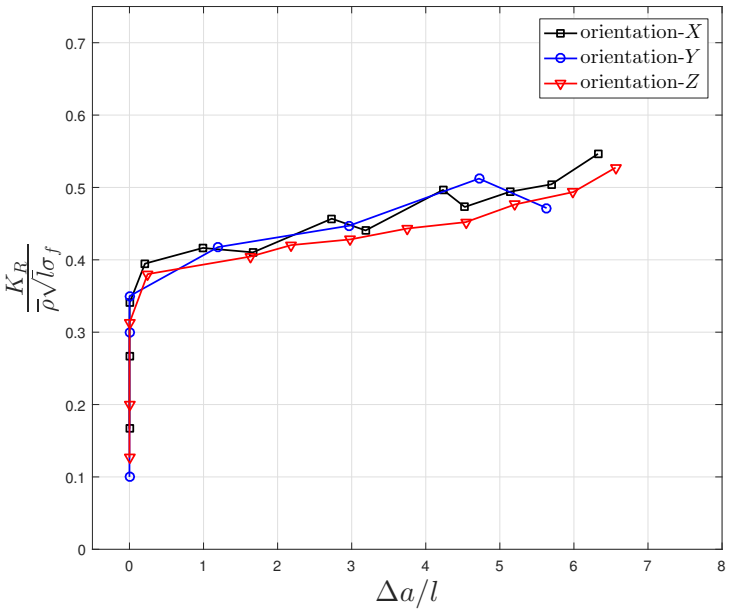

Figure 21: The fracture resistance curve for CT models.

6. Conclusions

The modulus, strength and fracture toughness of the octet-truss lattice were calculated using very high resolution FE models with isotropic base material properties and a brittle fracture criterion. The lattice strength was found to be highly sensitive to orientation compared to the modulus and the fracture toughness. The highest strength was seen in the orientation-Z structure, where it was double that of the orientation-Y structures and 35% higher than the orientation-X structures. When model size is sufficiently large, the modulus of orientation-X, orientation-Y and orientation-Z structures were almost identical.

In general, LEFM can be adequately used for lattice models with linear crack fronts. However, the toughness evaluated from the thumbnail crack model was significantly different compared to the value obtained from CT, SENT and SENB models due to the differences of structure configuration at the crack tip. The influence of T-stress on the toughness has been illustrated. The toughness increase linearly with T-stress for $T < T_c$, while for $T > T_c$, the further increase in T-stress resulted in a reduction in the toughness.

Although the fracture toughness was found to be almost isotropic, the crack paths strongly depend on the lattice orientation. In CT and SENT models, the crack paths for the orientation-Y structures were 60° to the loading direction, while the crack paths were horizontal in the orientation-X and Z structures. The thumbnail crack exhibited complex crack paths for the three orientations, particularly for orientation-Z, where the crack path was conical. An increase in fracture load was observed during crack growth which was attributed to the formation of a stronger structure configuration at the crack tip after removal of the most heavily loaded struts.

7. Acknowledgments

We acknowledge the use of the computational facilities of the Advanced Computing Research Centre, University of Bristol, `https://www.acrc.bris.ac.uk`.

References

[1] N. Wicks, J. W. Hutchinson, Optimal truss plates, International Journal of Solids and Structures 38 (2001) 5165–5183.

[2] S. Arabnejad, R. B. Johnston, J. Ann, B. Singh, M. Tanzer, D. Pasini, Acta Biomaterialia High-strength porous biomaterials for bone replacement : A strategy to assess the interplay between cell morphology , mechanical properties , bone ingrowth and manufacturing constraints, Acta Biomaterialia 30 (2016) 345–356.

[3] E. C. Wai-fah, Structural Engineering Handbook-Space Frame Structures, 3rd Edition, ASME Press, New York, 2000.

[4] P. Heinl, L. Mu, R. F. Singer, F. A. Mu, C. Ko, Cellular Ti – 6Al – 4V structures with interconnected macro porosity for bone implants fabricated by selective electron beam melting, Acta Biomaterialia 4 (2008) 1536–1544.

[5] Z. Xiaoyu, L. Howon, e. Weisgraber, Ultralight, ultrastiff mechanical metamaterials, Science 344 (6190) (2014) 1373–1377.

[6] S. Maiti, L. Gibson, M. Ashby, Deformation and energy absorption diagrams for cellular solids, Acta Metallurgica 32 (1984) 1963 – 1975.

[7] V. S. Deshpande, M. F. Ashby, N. A. Fleck, Foam topology: Bending versus stretching dominated architectures, Acta Materialia 49 (6) (2001) 1035–1040.

[8] A.-J. Wang, D. L. McDowell, In-Plane Stiffness and Yield Strength of Periodic Metal Honeycombs, Journal of Engineering Materials and Technology 126 (2) (2004) 137–156.

[9] J. Wallach, L. Gibson, Mechanical behavior of a three-dimensional truss material, International Journal of Solids and Structures 38 (2001) 7181 – 7196.

[10] V. Deshpande, N. Fleck, M. Ashby, Effective properties of the octet-truss lattice material, Journal of the Mechanics and Physics of Solids 49 (2001) 7181 – 7196.

[11] L. Dong, V. Deshpande, H. Wadley, Mechanical response of ti–6al–4v octet-truss lattice structures, International Journal of Solids and Structures 60-61 (2015) 107 – 124.

[12] H. Gu, M. Pavier, A. Shterenlikht, Experimental study of modulus, strength and toughness of 2d triangular lattices, International Journal of Solids and Structures 152-153 (2018) 207 – 216.

[13] M. O'Masta, L. Dong, L. St-Pierre, H. Wadley, V. Deshpande, The fracture toughness of octet-truss lattices , Journal of the Mechanics and Physics of Solids 98 (2017) 271 – 289.

[14] E. W. Andrews, G. Gioux, P. Onck, L. J. Gibson, Size effects in ductile cellular solids part ii : experimental results, International Journal of Mechanical Sciences 43 (2001) 0–1.

[15] I. Schmidt, N. A. Fleck, Ductile fracture of two-dimensional cellular structures, International Journal of Fracture 111 (4) (2001) 327–342.

[16] N. H.C.Tankasala, V.S.Deshpande, Crack-tip Fields and Toughness of Two-Dimensional Elasto-plastic Lattices, Journal of Applied Mechanics 82 (2015) 1–10.

[17] F. N. A., Q. XinMing, The damage tolerance of elastic-brittle, two-dimensional isotropic lattices, Journal of the Mechanics and Physics of Solids 55 (3) (2007) 562–588.

[18] J. S. Huang, L. J. Gibson, Fracture toughness of brittle honeycombs, Acta metallurgica et materialia 39 (7) (1991) 1617–1626.

[19] X. Cui, Z. Xue, Y. Pei, D. Fang, Preliminary study on ductile fracture of imperfect lattice material, International Journal of Solids and Structures 48 (25-26) (2011) 3453–3461.

[20] X. L. Wang, W. J. Stronge, Micropolar theory for two-dimensional stresses in elastic honeycomb, Proceedings of the Royal Society of London. Series A: Mathematical, Physical and Engineering Sciences 455 (1999) 2091–2116.

[21] S. Elangovan, B. Altan, G. Odegard, An elastic micropolar mixture theory for predicting elastic properties of cellular materials, Mechanics of Materials 40 (2008) 602 – 615.

[22] M. François, L. Chen, M. Coret, Elasticity and symmetry of triangular lattice materials, International Journal of Solids and Structures 60-61 (2017) 129.

[23] ABAQUS/CAE user's manual : version 6.14., ABAQUS.Inc., 2014.

[24] T.L.Anderson, Fracture Mechanics: Fundamentals and Applications, 4th Edition, CRC Press, 2017.

[25] D. Gross, T. Seelig, Fracture Mechanics, 2nd Edition, Springer-Verlag Berlin Heidelberg, 2011.

[26] ASTM E399 - 17-Standard Test Method for Linear-Elastic Plane-Strain Fracture Toughness KIc of Metallic Materials, American Society for Testing and Materials.

[27] S. K. Kudari, K. G. Kodancha, 3d stress intensity factor and t-stresses (t11 and t33) formulations for a compact tension specimen, Fracture and Structural Integrity 11 (39).

[28] J. Huang, L. Gibson, Analysis of constraint in single edge notch tension specimens using the t-stress, International Journal of Pressure Vessels and Piping 65 (1) (1996) 13 – 19.

[29] X. Wang, Elastic t-stress for semi-elliptical surface cracks in finite thickness plates 70 (2003) 731–756.

[30] H. T. G. R.Irwin, The Stress Analysis Of Cracks Handbook, 3rd Edition, ASME Press, New York, 2000.